scientific reports

OPEN

In the quest of lossless slow light at surface plasmons

Korlan Ziyatkhan[1], Bakhtiyar Orazbayev[1✉] & Constantinos Valagiannopoulos[2✉]

Surface plasmons, namely, the waves guided at the boundaries between metals and dielectrics, are employed in a variety of engineering applications, spanning from photodetection and near-field scanning to biosensing and medical imaging. The spatial confinement of this effect makes it ideal for a quest towards low-loss guiding of slow light along the interfaces of similar heterostructures. Numerous pairs of materials are considered to determine the conditions for the emergence of strong surface waves, once the visible-light frequency is selected to secure minimum phase velocity or minimum propagation losses. The reported results can offer multiple optimal alternatives in the forward and inverse design of photonic components calling for high-intensity, low-loss slow light being guided across two-dimensional boundaries.

A major discovery in the electromagnetics research of the previous century was the observation of surface waves across a metal-dielectric interface with arbitrarily large wavenumber. They are called surface plasmons and refer to trapped electromagnetic fields between the two media because of their interaction with the free electrons of the conductor[1]. Such a spatial concentration of the photonic signal was first demonstrated as a matching regime between thin metallic films and free space[2] while the frequency dispersion of supported modes was identified subsequently[3]. The reported effects call for feeding by evanescent waves into a vacuum and, thus, they get better illustrated in free-standing structures involving total internal reflection like the prisms of Otto[4] and Kretschmann[5]. Interestingly, some of the primitive utilities based on surface plasmons, concerned the accurate measurement of the optical constants for thin metal foils[6] and the suppression of damping for the developed propagated waves, in the vicinity of interfaces[7].

This type of surface waves and its technological implications established plasmonics, a new field in material science, where several old concepts from electronics are revolutionized. Indeed, within the plasmonics framework, the digital information sent from one point to another could travel with the speed of light[8]. Such a field made great strides, in terms of instrumentation development, across various fronts like resonant sensors[9], quantum light generators[10] near-field scanners[11] and data storage elements[12]. Importantly, sub-diffraction-limited optical imaging[13] and sharp photonic switching in biological[14], chemical[15], and medical[16] systems are just few applications of the same phenomenon. In addition, the influence of the shape of metallic nanoparticles on the intensity of surface plasmons has been studied[17] while the capacities of the effect in monitoring spectroscopically the molecular interactions in real time have been thoroughly examined[18,19]. Interestingly, similar surface waves can be observed not only across the boundary of metals but also at square holes opened on a conducting surface[20] or graphene monolayers sandwiched between two insulators[21].

The effect of surface plasmon keeps delivering surprising physics results and spinning out radical engineering applications. In particular, judiciously designed plasmonic nanostructures can greatly enhance light absorption by converting incident photons into hot electrons[22] or detecting molecules[23]. Surface plasmon setups enable also superior sensitivity in identifying refractive index[24], photodetection[25] and DNA molecule sensing[26]. Importantly, surface plasmon resonances allow for optimization of photoabsorbers and photothermal nanoheaters[27] while they can help understanding the activation mechanism of oxygen molecules[28]. Moreover, broadband excitation of these surface waves through rectangular waveguides exhibits a great potential in microwave circuit modeling[29], boosting nonlinearities[30] and catalysis engineering[31].

With the rise of metasurfaces, surface waves continue to yield groundbreaking physics insights and drive innovative technological solutions for wave manipulation, including the spoof surface plasmons[32]. Metasurfaces enable precise routing of electromagnetic signals[33], transforming wave properties through gradient metasurfaces for applications like beam shaping and imaging[34]. They also facilitate leaky wave mechanisms for efficient coupling into radiation modes[35], which is crucial for compact, high-performance antennas with dynamic beam steering. Additionally, they allow the creation of slow wave structures that enhance wave-matter interactions[36], improving the sensitivity in sensing applications and the performance in delay lines or nonlinear optical effects.

[1]Department of Physics, Nazarbayev University, Astana 010000, Kazakhstan. [2]School of Electrical and Computer Engineering, National Technical University of Athens, 15772 Athens, Greece. ✉email: bakhtiyar.orazbayev@nu.edu.kz; valagiannopoulos@ece.ntua.gr

These versatile properties, that are confined across only two dimensions, render metasurfaces essential for developing advanced photonic devices and terahertz systems. However, their fabrication is often complex and challenging, limiting their practical implementation and scalability.

In this work, we consider numerous pairs of metallic and dielectric media across the visible part of the frequency spectrum to find out which of them are able to host slow light of the highest quality via the developed surface plasmons when surrounded by a lossless dielectric, with no need of metasurfaces. Slow light, namely waves with small phase and group velocities, makes a very desirable feature that promotes stronger light-matter interactions[37], offers additional regulation of the operational spectral boundaries and allows for delaying and temporarily storing light in all-optical memories[38]. Usually slow light is observed at photonic crystals exploiting the dispersion inherited to the effective medium by the perforated structure[39]; moreover, the increased phase sensitivity is directly utilized towards decreasing the sizes of many devices, including switches, routers, logical gates, and wavelength converters[40]. In our study, this slow light effect is forced to occur at the interface of two materials. Therefore, the respective signals are expressed as enhanced surface waves which makes them more easily recordable without state-of-the-art equipment[41] and enables a massively parallelizable analog photonic processing across multiple interfaces.

In particular, we investigate two slabs from these media, connected back-to-back, while being unilaterally excited by oblique waves propagated into a dense dielectric matrix. Naturally, due to the opposite signs of the real parts of the two permittivities, the magnetic field gets locally maximized across the interface. We search for the wavelength that leads to either the slowest or the least lossy plasmonic resonance and optimize the dimensions of the layers to give the largest field enhancement at their common boundary. In this sense, the obtained optimal layouts meet the necessary requirements to guide strong waves that are spatially confined to the interface. The reported designs are translated to extra degrees of freedom in the fabrication process of setups serving a wide range of applications from optical sensing and field localization to chemical reaction monitoring and data storage. Indeed, multiple alternative and efficient solutions are available, from which one may pick those that respect additional constraints such as media availability, construction cost or chemical compatibility and stability.

Results
Problem statement

We consider the simplest possible structure of two thin adjacent slabs with sizes h_1 and h_2, respectively (see Fig. 1a, where the Cartesian coordinate system (x, y, z) is also defined). The two rectangular regions are filled with materials of relative complex permittivities ε_1 and ε_2, respectively. The whole structure is placed into a lossless dielectric of relative permittivity $\varepsilon \gg 1$, where the exciting wave travels along a direction that makes angle θ with the normal-to-interface axis. The incident magnetic field expressed as $\mathrm{H}_{\mathrm{inc}} = \hat{y} \exp(-\mathrm{i}k_0 z \sqrt{\varepsilon} \cos\theta - \mathrm{i}k_0 x \sqrt{\varepsilon} \sin\theta)$, of unitary magnitude 1 A/m. The symbol $k_0 = 2\pi/\lambda$ is used for the wavenumber into free space; similarly, (ε_0, μ_0) correspond to the permittivity and permeability of vacuum. Harmonic time dependence of the form $\exp(+\mathrm{i}\omega t)$ is used and suppressed throughout the analysis, where $\omega = 2\pi/(\lambda\sqrt{\varepsilon_0\mu_0}) = 2\pi c/\lambda$ is the angular frequency of the signals and $c = 1/\sqrt{\varepsilon_0\mu_0}$ is the speed of light into vacuum.

As mentioned above, such a structure has been used to formulate the principles of a major discovery in the research on matter-wave interactions, in the midst of the last century: the surface plasmon resonance[1–3]. In particular, it was found that at an interface between two media whose real parts of dielectric functions are of opposite sign $(\mathrm{Re}[\varepsilon_1]\mathrm{Re}[\varepsilon_2] < 0)$, coherent electron oscillations can be hosted. In this way, surface waves across the boundary are excited with magnetic field along y axis and propagation along x axis obeying to a factor
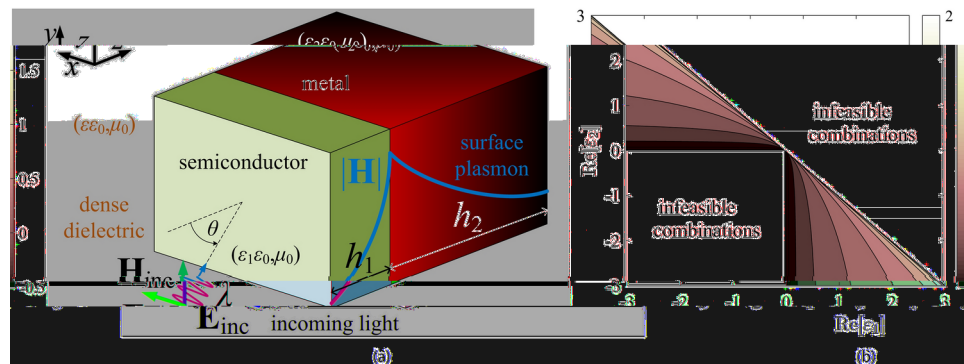

Figure 1. (**a**) A simple bilayer comprising a semiconducting slab of thickness h_1 and relative permittivity ε_1 as well as a metallic layer of thickness h_2 and relative permittivity ε_2. The structure is placed into a dense dielectric of relative permittivity ε and gets obliquely illuminated by a plane wave of light with wavelength λ that propagates along a direction making angle θ with the normal direction. The setup is designed to host surface plasmon resonances regarding the magnetic field magnitude $|\mathrm{H}(z)|$ along the interface between the two media $(z = 0)$. (**b**) The variation of the decimal logarithm of the normalized propagation constant $\log(\beta/k_0)$ across the map of the two permittivities $(\varepsilon_1, \varepsilon_2)$ of the used media. Lossless designs are considered $(\mathrm{Im}[\varepsilon_1] = \mathrm{Im}[\varepsilon_2] = 0)$.

$\exp(-\mathrm{i}\beta x)$. That breakthrough enabled information transfer at the nanoscale, similarly to photonics but by means of surface plasmons; thus, the respective research area is referred to as plasmonics.

Importantly, the demand for dying fields away from the interface ($z = 0$), forces the propagation constant β to be given by:

$$\beta \equiv \mathrm{Re}[\beta](1 - \mathrm{i}\,\tan\delta) = k_0 \sqrt{\frac{\varepsilon_1\varepsilon_2}{\varepsilon_1 + \varepsilon_2}}, \tag{1}$$

which routinely leads to slower waves than those traveling into vacuum ($\beta > k_0$). Indeed, in Fig. 1b, we represent the decimal logarithm of the normalized propagation constant $\log(\beta/k_0)$ with respect to the permittivities $(\mathrm{Re}[\varepsilon_1], \mathrm{Re}[\varepsilon_2]) = (\varepsilon_1, \varepsilon_2)$ in a lossless scenario ($\mathrm{Im}[\varepsilon_1] = \mathrm{Im}[\varepsilon_2] = 0$). It is clear that the conditions $\varepsilon_1\varepsilon_2 < 0$ and $\varepsilon_1 + \varepsilon_2 < 0$ should be mutually satisfied, while the represented quantity increases unboundedly as one approaches the line $\varepsilon_2 = -\varepsilon_1$. However, the employed materials, and especially the epsilon-negative metals, are characterized by losses which inherits β with an imaginary part. As indicated in (1), the propagating surface wave exhibits losses expressed by the quantity $\tan\delta = -\mathrm{Im}[\beta]/\mathrm{Re}[\beta]$.

It should be stressed that, in order for a surface wave to be developed at $z = 0$ of Fig. 1a, the excitation should have components with the same x-dependence, namely, $\exp(-\mathrm{i}\beta x)$. It can be achieved if evanescent incoming waves are created with use of certain configurations like Otto[4] and Kretschmann[5] prisms. However, we certainly can observe the effect for the obliquely incident plane wave of Fig. 1a, as long as:

$$\sqrt{\varepsilon} = \frac{\mathrm{Re}[\beta]}{k_0 \sin\theta}, \tag{2}$$

for low-loss plasmons. One may point out that slow propagation of light is by default feasible, in case dense dielectrics with $\varepsilon \gg 1$ are available, as indicated in (2); importantly, $\mathrm{Re}[\beta] < \sqrt{\varepsilon}$ since the surface plasmon is fed only by the parallel to x axis wavenumber. Indeed, the developed surface plasmon has larger phase velocity $v \equiv \omega/\mathrm{Re}[\beta] = c/(\sqrt{\varepsilon}\sin\theta)$ than that of a plane wave traveling into the background medium ($c/\sqrt{\varepsilon}$). However, we aim at compressing slow light along the interface of two media and, to achieve this, we used as vessel the well-known surface plasmons. The reason for such a choice pertains to the squeezed nature of surface effects that admits the parallelization of photonic signal processing while being behind the idea to use collectively several interfaces, one feeding the next one.

Thus, a good indicator of the intensity of the effect would be the squared magnitude of the magnetic field evaluated at the boundary $z = 0$, compared with the respective quantity at the front interface $z = -h_1$. In this sense, we can define our metric $Q \equiv |\mathrm{H}(0)|^2/|\mathrm{H}(-h_1)|^2$ which should be optimized when searching for the most powerful surface wave. We impose the necessary boundary conditions at $z = -h_1, 0, h_2$ and the magnetic field everywhere in space is determined. In this way, the considered metric takes the form:

$$Q = \frac{2\kappa_1\varepsilon_2}{e^{-\kappa_1 h_1}(\kappa_1\varepsilon_2 - \kappa_2\varepsilon_1) + e^{+\kappa_1 h_1}(\kappa_1\varepsilon_2 + \kappa_2\varepsilon_1) - 2e^{-\kappa_2 h_2}\kappa_2 s_1\varepsilon_1 \frac{\kappa_2\sqrt{\varepsilon} - \mathrm{i}k_0\varepsilon_2\cos\theta}{\kappa_2 c_2\sqrt{\varepsilon} + \mathrm{i}k_0\varepsilon_2 s_2\cos\theta}}, \tag{3}$$

where $c_j = \cosh(\kappa_j h_j)$ and $s_j = \sinh(\kappa_j h_j)$ for $j = 1, 2$. The symbols $\kappa_j = k_0\sqrt{\varepsilon\sin^2\theta - \varepsilon_j}$ describe the waves into each material ($j = 1, 2$). The first layer will be the semiconducting one and the second the metallic one since, otherwise, the penetration to the interface will be poor[42]. Indeed, due to the huge textural mismatch between air and the metallic layer, such a choice would lead to substantial reflections back to the source[43]. On the contrary, if $\mathrm{Re}[\varepsilon_1] > 0$ with relatively suppressed thermal effects ($|\mathrm{Im}[\varepsilon_1]| \ll \mathrm{Re}[\varepsilon_1]$), the dielectric slab of suitable size h_1 will match the incoming wave, minimize reflectivity and enable the magnetic field to concentrate across the boundary[44].

Our mission would be to maximize the metric Q by respecting additional constraints related to the propagation constant β of the surface wave, as defined by (1). In Fig. 2a, we show the typical variation of Q from (3) across the map of the physical thicknesses of the two layers (h_1, h_2); the obtained pattern is practically independent from the incidence angle θ since the metric Q measures a relative signal level at $z = 0$ compared to the respective entry quantity at $z = -h_1$. One directly observes that there is an optimal size h_1 that maximizes Q while the influence of the thickness of the metallic layer h_2 is rather weak; for this reason, we fix that parameter at $h_2 = 200$ nm which is enough to capture the global maximum in most designs. As far as the incoming angle θ is concerned, it is picked based on how substantial is the ratio $|\mathrm{H}(0)|/|\mathrm{H}_{\mathrm{inc}}|$, where $|\mathrm{H}_{\mathrm{inc}}| = 1$ A/m.

In Fig. 2b, we represent that quantity with respect to the physical size of the dielectric h_1 and the angle θ; we also realize that the field strength appears at $\theta \cong 45°$ which would also be our choice in the considered examples. The additional constraints concern how slow and how low-loss are the surface waves that may be developed across the interface. In particular, in the quest of slow plasmons, we will study the system for an operational wavelength λ at which the normalized propagation constant $\mathrm{Re}[\beta/k_0] > 0$ from (1) becomes maximum. Similarly, when searching for the least lossy plasmons, we will pick a wavelength λ, where the loss tangent $\tan\delta > 0$, again from (1), gets minimized.

The quantity $\mathrm{Re}[\beta/k_0]$ equals to the confinement factor of the surface plasmon, which represents (in dimensionless terms) the reduced plasmon phase velocity relative to the speed of light, namely, expresses the wavelength shrinkage to lengths smaller than that of a free-space photon[45]. As far as the losses $\tan\delta$ are
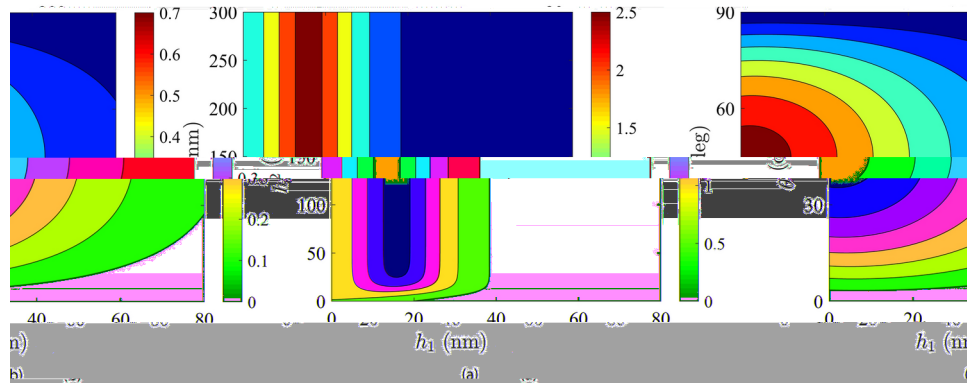
Figure 2. (**a**) Typical variation of metric $Q \equiv |\mathrm{H}(0)|^2/|\mathrm{H}(-h_1)|^2$, as defined by (3), with respect to the thickness h_1 of the semiconducting layer and the thickness h_2 of the metallic layer. The response is practically independent from the angle of incidence θ due to the implicit permittivity selection (2) and the relative nature of metric Q. (**b**) Typical representation of relative magnetic field $|\mathrm{H}(0)|/|\mathrm{H}_{\mathrm{inc}}|$, with respect to the thickness h_1 of the semiconducting layer and the incidence angle θ. Note that ε varies with respect to θ, according to (2).

concerned, they are inversely related to the propagation length which equals to $1/(2\mathrm{Im}[\beta])$ and shows how weak is the damping of the developed surface wave[46]. In this sense, the quantities that will be optimized in the following are neither new nor original; however, the simultaneous optimization of the relative strength Q of the field concentration across the interface certainly is a feature that leads to meaningful results. Another novel aspect of our research has to do with the consideration of a set of available media, that can be arbitrarily expanded, to provide upper limits for the related performances across the regarded visible-light spectrum. In this way, multiple alternatives of bilayers are given to the designer that are optimally operated at different bands. Hence, extra degrees of freedom enrich the fabrication and testing processes which will be executed despite emerged availability, cost or compatibility constraints.

We expect that our study will inspire further experimental efforts to develop slow light at interfaces between several couples of media in bilayer configurations. In an analogous fashion, alternative plasmonic materials[47] have been compiled to provide advantages in device performance, design flexibility, fabrication, integration, and tunability. Especially for slow light, our study can have an impact by offering several successful designs towards electromagnetically induced transparency in optomechanical considerations[48] and tunable all-optical delays in optical fibers[49]. Importantly, the provided multiple alternative bilayers being able to host vanishing wave velocities, can be critical towards enabling the development of whispering-gallery modes in microgear photonic crystal rings[50] or studying topological effects with counter-propagating waves for the active control on a chip[51].

Optimal material pairs

This strategy will be adopted in the following numerical results, where the quest for strong surface plasmon resonances takes place. In particular, we will consider a list of ordinary semi-conductors (ε_1) including elements like carbon and crystalline silicon or compounds like arsenides and phosphides, which exhibit significant dispersion in the visible (400 nm $< \lambda <$ 700 nm). When it comes to the plasmonic rear layer (ε_2), we regard a set of commonly used metals of various levels of $\mathrm{Im}[\varepsilon_2]$, under visible light. The outcome of our optimizations is presented in Tables 1 and 2, where all the combinations of the aforementioned materials are examined: each dielectric corresponds to one row and each metal to one column with increasing losses from silver (least lossy) to permalloy (most lossy). Each box of both the Tables is color-coded to the corresponding wavelength of visible light at which optimal plasmons arise. In addition, the field enhancement metric Q, the maximum relative propagation constant $\mathrm{Re}[\beta/k_0]$ or the minimum loss tangent $\tan\delta$, together with the operational wavelength λ are mentioned for each couple of media.

In Table 1, where the optimization results regarding $\mathrm{Re}[\beta/k_0]$ are presented, we clearly see that numerous pairs of materials lead to slow light over two dozen times stronger than the incoming field. Thus, Table 1 can serve as a library of optimal designs that can absorb any deficiencies in a laboratory regarding the availability of materials or cost of fabrication. It can be noticed that the plasmons able to develop across the interface between two layers can be up to 95 times slower than the electromagnetic waves into free space (GaP/Ag bilayer). It should be remarked that the superiority of that specific design could not be predicted based on the mild lossy behavior of both the incorporated media due to the following reasons. (i) The recommended frequency of operation ($\lambda = 538$ nm) does not coincide with that minimizing the overall losses of the two materials. (ii) Other designs exhibit much higher performance Q at alternative wavelengths than the one that GaP/Ag bilayer is optimally working.

One can also observe the preference of silver-based designs for yellow color, the trend of platinum-based bilayers to host plasmons at the green color of the visible spectrum, and a similar behavior of copper, gold, titanium and permalloy regarding red color, as well. Interestingly, for structures comprising aluminum, it is the dielectric that decides at which band the setup will be operated in an optimal manner, and, in most cases, it regards blue rays. It should be also noted that suitably backed carbon and gallium phosphide semiconducting

	Silver		Copper	Gold	Platinum	Titanium	Aluminium	Permalloy
$Q \cong$ 2.2, $\text{Re}[\beta/k_0] \cong$ 3.00, ...00 nm	$Q \cong 2.2$, $\text{Re}[\frac{\beta}{k_0}] \cong 2.53$, $\lambda = 509$ nm	**Carbon (C)**	$Q \cong 63.5$, $\text{Re}[\frac{\beta}{k_0}] \cong 10.78$, $\lambda = 431$ nm	$Q \cong 8.6$, $\text{Re}[\frac{\beta}{k_0}] \cong 4.16$, $\lambda = 582$ nm	$Q \cong 8.9$, $\text{Re}[\frac{\beta}{k_0}] \cong 4.32$, $\lambda = 557$ nm	$Q \cong 4.4$, $\text{Re}[\frac{\beta}{k_0}] \cong 3.12$, $\lambda = 426$ nm	$Q \cong 2.1$, $\text{Re}[\frac{\beta}{k_0}] \cong 2.45$, $\lambda = 620$ nm	$Q \cong$, $\text{Re}[\frac{\beta}{k_0}] \cong$, $\lambda = 4$...
$\cong 7.92$, ...58 nm	$Q \cong 2.1$, $\text{Re}[\frac{\beta}{k_0}] \cong 3.31$, $\lambda = 695$ nm	**Silicon (Si)**	$Q \cong 66.0$, $\text{Re}[\frac{\beta}{k_0}] \cong 17.30$, $\lambda = 594$ nm	$Q \cong 36.7$, $\text{Re}[\frac{\beta}{k_0}] \cong 12.79$, $\lambda = 662$ nm	$Q \cong 33.3$, $\text{Re}[\frac{\beta}{k_0}] \cong 12.61$, $\lambda = 651$ nm	$Q \cong 8.9$, $\text{Re}[\frac{\beta}{k_0}] \cong 7.47$, $\lambda = 510$ nm	$Q \cong 1.9$, $\text{Re}[\frac{\beta}{k_0}] \cong 3.61$, $\lambda = 695$ nm	$Q \cong$, $\text{Re}[\frac{\beta}{k_0}] \cong$
4.2, $\cong 6.16$, 506 nm	$Q \cong 2.1$, $\text{Re}[\frac{\beta}{k_0}] \cong 3.81$	**Aluminium Antimonide (AlSb)**	$Q \cong 33.5$, $\text{Re}[\frac{\beta}{k_0}] \cong 13.02$, $\lambda = 605$ nm	$Q \cong 31.9$, $\text{Re}[\frac{\beta}{k_0}] \cong 11.89$, $\lambda = 666$ nm	$Q \cong 28.3$, $\text{Re}[\frac{\beta}{k_0}] \cong 11.46$	$Q \cong 6.0$, $\text{Re}[\frac{\beta}{k_0}] \cong 6.72$, $\lambda = 537$ nm	$Q \cong 1.9$, $\text{Re}[\frac{\beta}{k_0}] \cong 3.61$	$Q \cong$, $\text{Re}[\frac{\beta}{k_0}]$
$\cong 3.6$, $\cong 5.54$, $= 490$ nm	$Q \cong 1.9$, $\text{Re}[\frac{\beta}{k_0}] \cong 3.67$, $\lambda = 700$ nm	**Gallium Arsenide (GaAs)**	$Q \cong 12.8$, $\text{Re}[\frac{\beta}{k_0}] \cong 8.41$, $\lambda = 605$ nm	$Q \cong 13.8$, $\text{Re}[\frac{\beta}{k_0}] \cong 8.28$, $\lambda = 668$ nm	$Q \cong 12.9$, $\text{Re}[\frac{\beta}{k_0}] \cong 8.15$, $\lambda = 669$ nm	$Q \cong 4.5$, $\text{Re}[\frac{\beta}{k_0}] \cong 5.75$, $\lambda = 529$ nm	$Q \cong 1.7$, $\text{Re}[\frac{\beta}{k_0}] \cong 3.48$, $\lambda = 700$ nm	$Q \cong$, $\text{Re}[\frac{\beta}{k_0}]$
$\cong 2.2$, $\cong 4.72$, $= 559$ nm	$Q \cong 1.5$, $\text{Re}[\frac{\beta}{k_0}] \cong 3.44$, $\lambda = 700$ nm	**Indium Arsenide (InAs)**	$Q \cong 4.8$, $\text{Re}[\frac{\beta}{k_0}] \cong 5.79$, $\lambda = 654$ nm	$Q \cong 5.3$, $\text{Re}[\frac{\beta}{k_0}] \cong 5.63$, $\lambda = 700$ nm	$Q \cong 5.2$, $\text{Re}[\frac{\beta}{k_0}] \cong 5.66$, $\lambda = 700$ nm	$Q \cong 2.7$, $\text{Re}[\frac{\beta}{k_0}] \cong 4.98$, $\lambda = 581$ nm	$Q \cong 1.3$, $\text{Re}[\frac{\beta}{k_0}] \cong 3.28$, $\lambda = 700$ nm	$Q \cong$, $\text{Re}[\frac{\beta}{k_0}]$
$\cong 4.2$, $\cong 5.53$, $= 450$ nm	$Q \cong 2.2$, $\text{Re}[\frac{\beta}{k_0}] \cong 3.64$, $\lambda = 670$ nm	**Gallium Indium Phosphide (GaInP)**	$Q \cong 17.2$, $\text{Re}[\frac{\beta}{k_0}] \cong 8.60$, $\lambda = 567$ nm	$Q \cong 15.8$, $\text{Re}[\frac{\beta}{k_0}] \cong 8.63$, $\lambda = 656$ nm	$Q \cong 14.7$, $\text{Re}[\frac{\beta}{k_0}] \cong 8.34$, $\lambda = 656$ nm	$Q \cong 4.9$, $\text{Re}[\frac{\beta}{k_0}] \cong 5.49$, $\lambda = 505$ nm	$Q \cong 1.9$, $\text{Re}[\frac{\beta}{k_0}] \cong 3.46$, $\lambda = 676$ nm	$Q \cong$, $\text{Re}[\frac{\beta}{k_0}]$
$\cong 7.4$, $\cong 6.63$, $= 417$ nm	$Q \cong 2.2$, $\text{Re}[\frac{\beta}{k_0}] \cong 3.42$, $\lambda = 575$ nm	**Gallium Phosphide (GaP)**	$Q \cong 95.4$, $\text{Re}[\frac{\beta}{k_0}] \cong 18.00$, $\lambda = 538$ nm	$Q \cong 32.7$, $\text{Re}[\frac{\beta}{k_0}] \cong 10.42$, $\lambda = 619$ nm	$Q \cong 23.3$, $\text{Re}[\frac{\beta}{k_0}] \cong 8.98$, $\lambda = 618$ nm	$Q \cong 7.8$, $\text{Re}[\frac{\beta}{k_0}] \cong 6.14$, $\lambda = 473$ nm	$Q \cong 1.9$, $\text{Re}[\frac{\beta}{k_0}] \cong 3.26$, $\lambda = 620$ nm	$Q \cong$, $\text{Re}[\frac{\beta}{k_0}]$

Table 1. Optimal designs hosting the slowest (maximal $\text{Re}[\beta/k_0]$) surface plasmons. The enhancement metric $Q = |\text{H}(0)|^2/|\text{H}(-h_1)|^2$ from (3), is optimized.

	Titanium (Ti)	Silver (Ag)	Platinum (Pt)	Permalloy (Py)	Gold (Au)	Copper (Cu)
Carbon (C)	$Q \cong 2.1$, $\tan\delta \cong 0.12$, $\lambda = 700$ nm	$Q \cong 72.4$, $\tan\delta \cong 0.004$, $\lambda = 700$ nm	$Q \cong 13.4$, $\tan\delta \cong 0.01$, $\lambda = 700$ nm	$Q \cong 2.3$, $\tan\delta \cong 0.11$, $\lambda = 700$ nm	$Q \cong 34.4$, $\tan\delta \cong 0.01$, $\lambda = 700$ nm	$Q \cong 33.2$, $\tan\delta \cong 0.01$, $\lambda = 700$ nm
Germanium (Ge)	$Q \cong 1.5$, $\tan\delta \cong 0.59$, $\lambda = 700$ nm	$Q \cong 21.6$, $\tan\delta \cong 1.51$, $\lambda = 700$ nm	$Q \cong 4.3$, $\tan\delta \cong 0.23$, $\lambda = 700$ nm	$Q \cong 1.7$, $\tan\delta \cong 0.60$, $\lambda = 700$ nm		
Gallium Indium Phosphide (GaInP)	$Q \cong 1.9$, $\tan\delta \cong 0.27$, $\lambda = 700$ nm	$Q \cong 76.1$, $\tan\delta \cong 0.01$, $\lambda = 676$ nm	$Q \cong 12.2$, $\tan\delta \cong 0.02$, $\lambda = 700$ nm	$Q \cong 2.2$, $\tan\delta \cong 0.25$, $\lambda = 700$ nm	$Q \cong 28.6$, $\tan\delta \cong 0.04$, $\lambda = 700$ nm	$Q \cong 27.7$, $\tan\delta \cong 0.05$, $\lambda = 700$ nm
Gallium Phosphide (GaP)	$Q \cong 2.0$, $\tan\delta \cong 0.23$, $\lambda = 700$ nm	$Q \cong 62.7$, $\tan\delta \cong 0.01$, $\lambda = 700$ nm	$Q \cong 12.5$, $\tan\delta \cong 0.02$, $\lambda = 700$ nm	$Q \cong 2.2$, $\tan\delta \cong 0.22$, $\lambda = 700$ nm	$Q \cong 29.6$, $\tan\delta \cong 0.03$, $\lambda = 700$ nm	$Q \cong 28.6$, $\tan\delta \cong 0.03$, $\lambda = 700$ nm

Table 2. Optimal designs hosting the least lossy (minimal $\tan\delta = |\text{Im}[\beta]|/\text{Re}[\beta]$) surface plasmons. The enhancement metric $Q = |\text{H}(0)|^2/|\text{H}(-h_1)|^2$ from (3), is optimized. Gray boxes correspond to poor performance Q.

slabs can support slow surface waves even at short wavelengths corresponding to the violet part of the spectrum. Additionally, among the various pairings, silicon and aluminium antimonide demonstrate the most favorable results when combined with several metals while the silicon/silver couple yields very high enhancement Q and, at the same time, a substantial wavenumber of $\text{Re}[\beta/k_0] \cong 17.3$ (second only to GaP/Ag design).

In the context of investigating minimally lossy plasmons, Table 2 presents a comprehensive compilation of results analogous to Table 1 but focusing on minimum $\tan\delta$ this time. Once again, every cell of Table 2 is associated with the wavelength of visible light, at which plasmons exhibit minimal loss. By inspection of Table 2, one sees that all the successful records (gray-colored boxes indicate poor performance Q) concerns red light excitation. Indeed, the higher the oscillating frequency gets, the more suppressed the losses become; it is not a coincidence that the vast majority of the designs prefer the largest possible wavelength $\lambda = 700$ nm of our

visible band. When it comes to the used media, once again bilayers with silver screen exhibit the highest signal enhancements at the semiconductor/metal interface ($z = 0$) compared to the entry level at $z = -h_1$. On the other hand, both phosphides (GaInP and GaP) and carbon deliver very successful designs when paired with gold and copper; in this way, the number of alternative bilayers that host highly-efficient surface plasmons gets increased significantly. Special mention deserves to C/Ag bilayers that deliver a giant relative strength $Q > 72$, combined with almost lossless behavior ($\tan \delta = 0.004$).

The Tables 1 and 2 contain the bilayers leading to the most enhanced surface plasmons that achieve the slowest phase velocities and the weakest thermal effects respectively, given the list of materials that one has available. A higher score is only feasible if additional media are employed or more complicated structures are incorporated; in this sense, the setups described by Tables 1 and 2 work in the best possible way and the exhibited performances constitute upper bounds characterizing the functionality of such a simplistic layout. Indeed, only hybrid optical waveguides, comprising dielectric nanowires in the vicinity of a metallic surface, lead to stronger coupling between the two parts and enable energy storage allowing for effective sub-wavelength transmission in non-plasmonic regions[52]. In addition, these unique optical properties of metallic nanostructures enable routing and manipulation of light at the nanoscale[53] that pave the way towards applications in light-emitting diodes, solar cells, low threshold laser, biomedical detection, and quantum information processing[54]. Similarly, nanochips based on surface plasmons have been proposed to contain plasmonic circuits that are very efficient in performing basic operations such as switching, summation and Boolean algebra[55]. Finally, more sophisticated setups than the ones investigated in our study enable local detection of electromagnetic energy transport below the diffraction limit[56] and plasmonic lasing at the nanoscale[57].

With this work, we do not claim a trailblazing degree of novelty regarding the physical effects; as noted above, the surface plasmons and the related phenomena are well-known for many decades. On the other hand, we make a systematic engineering effort of optimizing this simple setup and give an expandable catalog of structural components being able to host slow light across interfaces between two media; we advocate that such a compilation of optimal regimes is of some usefulness by itself. Furthermore, certain conclusions can be drawn regarding the highly-efficient layouts described by Tables 1 and 2. In Fig. 3a, we represent each and every design from Table 1 on the plane of real permittivities ($\mathrm{Re}[\varepsilon_1], \mathrm{Re}[\varepsilon_2]$) of the two media; each marker is painted in the color of visible light at which optimal operation is achieved. Naturally, the larger the $\mathrm{Re}[\varepsilon_1]$ gets, the more negative $\mathrm{Re}[\varepsilon_2]$ is needed so that β from (1) blows up. Bilayers operated at the violet color call for moderate $\mathrm{Re}[\varepsilon_1], |\mathrm{Im}[\varepsilon_1]|$ while the designs preferring green or blue color demand higher dielectric and plasmonic effects. In Fig. 3b, we show the optimized setups on the losses map ($\mathrm{Im}[\varepsilon_1], \mathrm{Im}[\varepsilon_2]$) of the two materials. It is clearly inferred that several designs from all colors of the visible spectrum are crammed at the upper right corner of the graph; therefore, we can say that the reported bilayers of Table 1 develop slow light combined by suppressed thermal effects.

Moreover, in Fig. 3c, we represent the contents of Table 2, working all under red illumination, on the same map as in Fig. 3a. It is noteworthy that the points are not scattered like in the case of slow light designs but form a line which can be characterized as a parametric boundary that gives low-loss plasmons. The locus comprises an almost vertical part where $\mathrm{Re}[\varepsilon_1]$ is smaller combined with less negative $\mathrm{Re}[\varepsilon_2]$ and an almost horizontal one declaring that most of the setups require $\mathrm{Re}[\varepsilon_2] \cong -5$ no matter what is the magnitude of $12 < \mathrm{Re}[\varepsilon_1] < 18$. That is another interesting feature hidden in the Table 2: visible-light surface plasmons with diminished losses change their behavior at a threshold of dielectric layer permittivity $\mathrm{Re}[\varepsilon_1] \cong 12$. In Fig. 3d, where the same layouts are shown across ($\mathrm{Im}[\varepsilon_1], \mathrm{Im}[\varepsilon_2]$) map, the results are even more meaningful. Again the formulated line is composed of a vertical and a horizontal part which match with the respective ones of Fig. 3c. In other words, the optimal designs into Table 2 either call for a plasmonic medium with $\varepsilon_2 \cong -5 - 5i$ combined with significantly lossy first layer or characterized by lower losses: $-5 < \mathrm{Im}[\varepsilon_2] < -1$ paired to lossless dielectrics.

Field spatial distribution

It would be informative to investigate the spatial distribution of the electromagnetic signal in order to demonstrate the concentration of the field across the interface between semiconducting and metallic layers. In Fig. 4, we choose some of the characteristic bilayers from Table 1 of slow surface plasmons and show the magnitude of the magnetic field, normalized by the unitary incoming magnitude $|\mathrm{H}(z)|/|\mathrm{H}_{\mathrm{inc}}|$. It is represented as a function
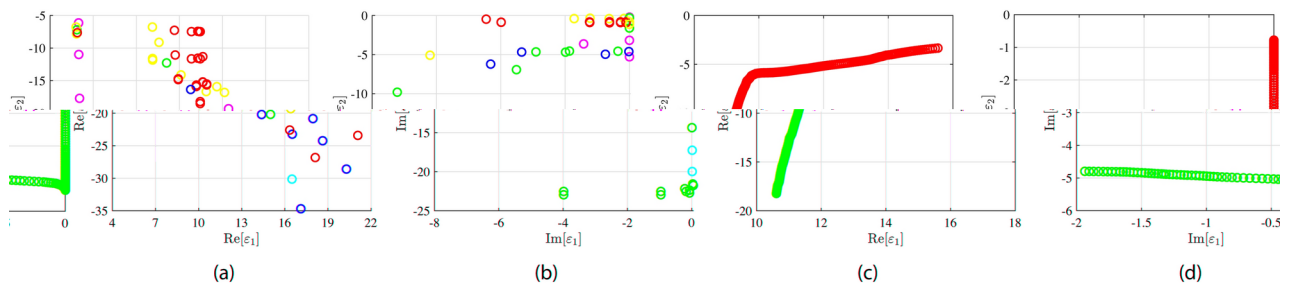

Figure 3. Representation of all the optimal designs from Tables 1 and 2 across planes of the constituent characteristics of the two media. Each marker is painted in the color of visible light at which optimal operation is achieved. (**a**) Bilayers of Table 1 across ($\mathrm{Re}[\varepsilon_1], \mathrm{Re}[\varepsilon_2]$) map, (**b**) bilayers of Table 1 across ($\mathrm{Im}[\varepsilon_1], \mathrm{Im}[\varepsilon_2]$) map, (**c**) bilayers of Table 2 across ($\mathrm{Re}[\varepsilon_1], \mathrm{Re}[\varepsilon_2]$) map, (**d**) bilayers of Table 2 across ($\mathrm{Im}[\varepsilon_1], \mathrm{Im}[\varepsilon_2]$) map.
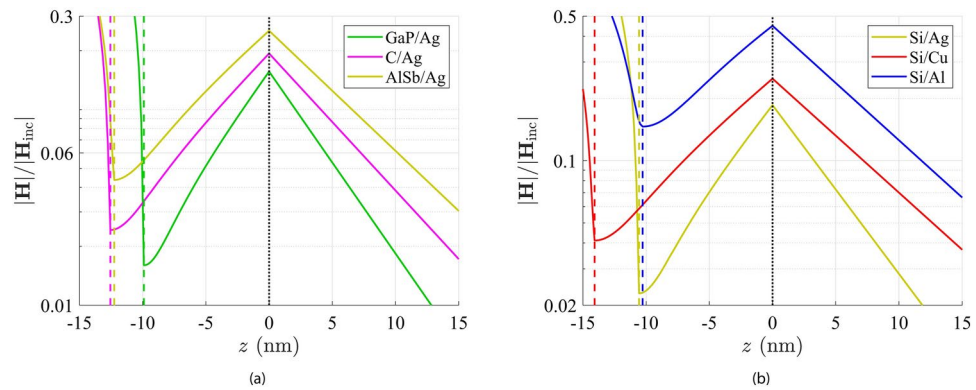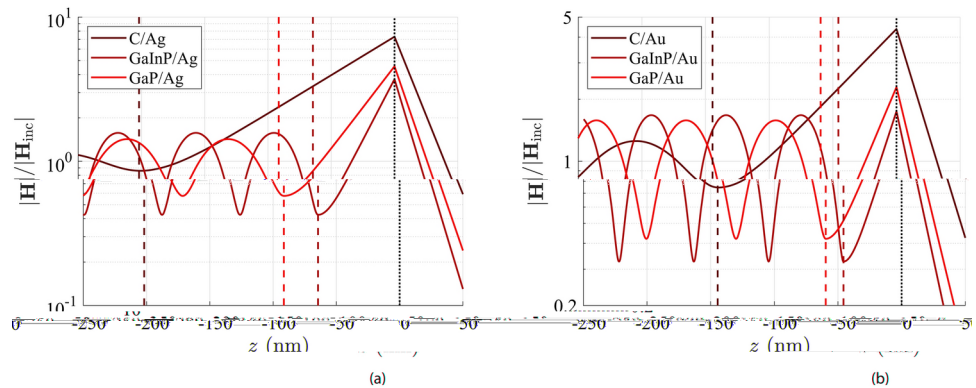
Figure 4. Variation of relative magnetic field magnitude $|H|/|H_{inc}|$ along axis z for: (**a**) Ag-based designs and (**b**) Si-based designs, operated at three different colors of the optical wavelengths λ, as indicated by the respective color of the curves. Maximum $\mathrm{Re}[\beta/k_0]$ bilayers are used from Table 1. Vertical black dashed lines denote the interface in-between the two media while colored dashed lines correspond to the front boundary of the used semiconducting slab.

Figure 5. Variation of relative magnetic field magnitude $|H|/|H_{inc}|$ along axis z for: (**a**) Ag-based designs operated at red color and (**b**) Au-based designs operated at three different colors of the optical wavelengths λ, as indicated by the respective color of the curves. Minimum $\tan\delta$ bilayers are used from Table 2. Dashed lines are sketched as in Fig. 4.

of the coordinate z in the vicinity of $z = 0$ and the color of each curve corresponds to the color of light under which the respective design works optimally. With colored dashed lines we indicate the respective front interface that meets first the incident wave while the black dashed line is used for the common surface between the two materials.

In Fig. 4a, we pick three silver-based designs working at the corresponding wavelengths of the visible light. In all the considered scenarios, the signal gets locally minimized when entering the structure and increases rapidly within the semiconducting part; this feature makes the setups befitted to operate as sensors that sustain Fano resonances. Such a behavior is related to half-wave loss; indeed hen light enters optically dense media from optically dilute media, the field strength usually becomes minimized at their interface. Once the wave penetrates the metallic layer, the signal decreases exponentially and exhibits a substantial maximum across the interface $z = 0$. The developed local field can be over nine times the magnitude of the incident wave. In Fig. 4b, we regard another triplet of designs that incorporate a silicon slab and similar conclusions are drawn; notice that the derivative of the represented quantity is not continuous at $z = 0$; it is an outcome of the different sign of the permittivities ($\mathrm{Re}[\varepsilon_1]\mathrm{Re}[\varepsilon_2] < 0$), as dictated by Fig. 1b. Interestingly, the magnetic field at $z = 0$ is a non-negligible fraction of the incident signal (30%–50%) which renders the device suitable to transform a sizable portion of the incident power into surface waves, within an ultrathin volume.

In Fig. 5a, we regard three of the most successful designs (all with silver mirrors) hosting low-loss plasmons from Table 2; as indicated above, they are all operated at red color ($\lambda = 700$ nm). One directly notices that the bilayers are much thicker than the ones of Fig. 4 achieving large $\mathrm{Re}[\beta/k_0]$. Indeed, losses are usually increasing with frequency and, inevitably, physical sizes get enlarged with wavelength. Due to the big spatial window we consider, one may observe the standing wave-like patterns into the dense dielectrics ($z < -h_1$), which are different for each case; the permittivity ε is proportional to the supported $\mathrm{Re}[\beta/k_0]$, as shown by (2). It is also noteworthy that the field at $z = 0$ is much stronger compared to the incident wave amplitude; such a finding

can be particularly important if local intensity enhancement is necessary for activation of nonlinearities and gyrotropies[58]. In Fig. 5b, we consider three scenarios materialized with gold-based setups and represent again the relative signal $|H|/|H_{inc}|$ as a function of normal coordinate z; the conclusions are similar with those drawn from Fig. 5a.

Wavelength dispersion

In Fig. 6a, we pick five designs from Table 1, where the slow surface plasmons are achieved, and represent the strength of their plasmons Q as a function of the operational wavelength λ across entire the visible part of wavelength spectrum. We notice that the points indicated by circular markers, which correspond to the optimal operations, do not necessarily coincide with the peaks of the curves. Indeed, the proposed wavelength is the one leading to maximum $\mathrm{Re}[\beta/k_0]$, not Q; that is why the operational points emerge at slightly higher λ. As expected from the scores included in Table 1, the most powerful surface wave is excited between gallium phosphide an silver layer, under green light illumination; on the contrary, the weakest plasmon appears at blue color within the Si/Al optimal bilayer. With Fig. 6a, we demonstrate the potential of our optimized designs to work as sharp filters for incoming light since they exhibit a single and significant resonance, each one at the prescribed color.

In Fig. 6b, we repeat the calculations of Fig. 6a but for designs taken from Table 2, where the least lossy plasmons are reported. It is obvious that all of them work under red light (optimized at the maximum visible wavelength $\lambda = 700$ nm), according to the results included in Table 2. Once again, huge scores Q are feasible when somehow shorter wavelengths are utilized, while substantial selectivity with respect to frequency is recorded since only red/infrared radiation is regarded (600 nm $< \lambda < 800$ nm), which is a much shorter band compared to that of Fig. 6a. Especially between carbon and silver, one can observe $Q > 130$, meaning that $|H(-h_1)| \to 0$; therefore , it makes an exceptional Fano-resonant filter with alternative utilities for switching and sensing.

In Fig. 7a, we consider the same layouts as in Fig. 6a but represent their response across a map whose horizontal axis indicates the $\mathrm{Re}[\beta/k_0]$ and vertical the basic metric Q, while the oscillation wavelength λ is implicitly swept, across the entire visible spectrum. It is clear that the selection of the slowest surface wave has been made for each design and, accordingly, the phase velocity of plasmons increase away from the optimal operational regime. Moreover, the relative intensity Q can be more significant for shorter λ but, beyond the represented peak, drops more rapidly.

In Fig. 7b, we show how the loss tangent $\tan\delta$ of the created surface wave changes when the oscillating wavelength is moving across the visible band, together with the well-known (from Figs. 6a, 7a) $Q = Q(\lambda)$ variation. Interestingly, if one increases the oscillating wavelength λ, one can achieve relatively powerful surface plasmons (high Q) combined with low losses (diminished $\tan\delta$). In this way, the robustness of all the beneficial features of the surface wave (substantial intensity Q, small phase velocity $\mathrm{Re}[\beta/k_0]$ and low losses $\tan\delta$) is directly demonstrated for a variety of working wavelengths λ.

In Fig. 8a, we regard the designs of Fig. 7b and represent their outputs on a performance map similar to Fig. 7a. Since one sweeps the visible part of the spectrum (400 nm $< \lambda < 700$ nm) and all the shown setups are optimized at $\lambda = 700$ nm, we assume only shorter wavelengths than the optimal one and, accordingly, we obtain function-like lines of bigger and bigger $\mathrm{Re}[\beta/k_0]$. As far as the metric Q from (3) is concerned, we record the same behavior of Fig. 6; in particular, the peak appears again at a wavelength shorter than the optimal, which is accompanied by a higher $\mathrm{Re}[\beta/k_0]$. Special mention deserves the extreme change in $\mathrm{Re}[\beta/k_0]$ exhibited by C/Ag bilayer, which also makes the most successful design. In Fig. 8b, we show the same setups but across the $(\tan\delta, Q)$ performance plane, where the least lossy features of the picked layouts is demonstrated. The similarity of the behavior of the curves between Fig. 8a, b is noteworthy which means that if one requires slower surface plasmons, inevitably has to cope with more pronounced thermal effects.
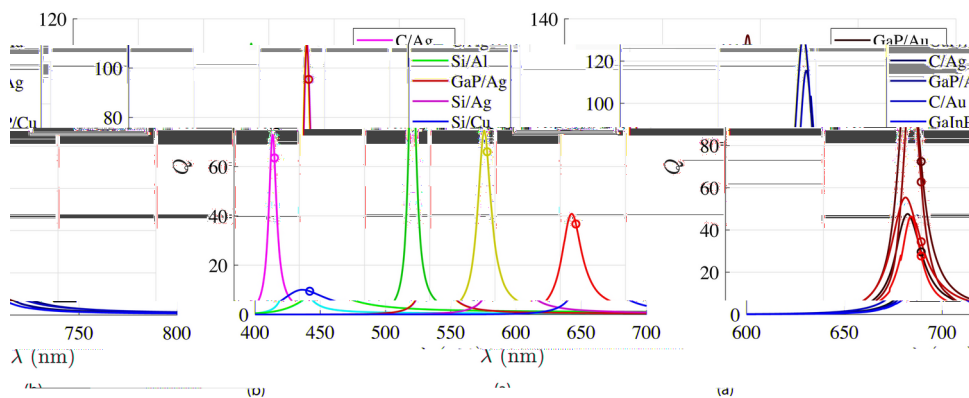

Figure 6. The enhancement metric Q as function of oscillating wavelength λ. (**a**) Bilayers from Table 1. (**b**) Bilayers from Table 2. The optimal points are denoted by circular markers. The colors of the curves indicate the respective color of the visible spectrum.
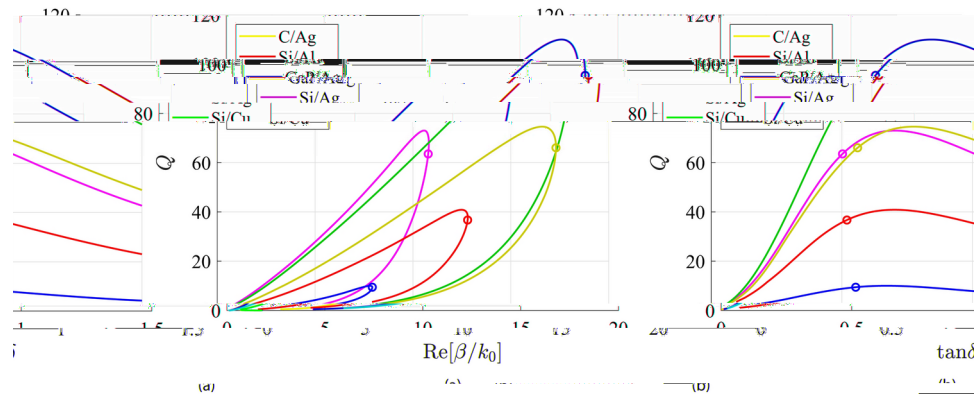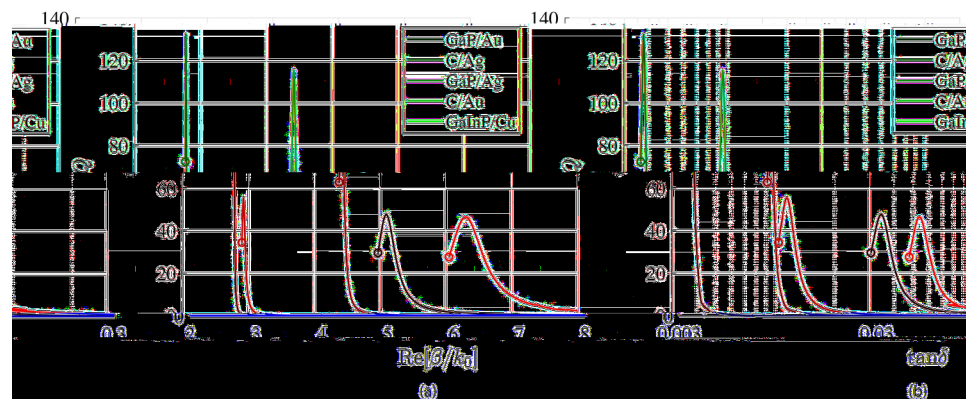
Figure 7. Trajectories of optimal designs from Fig. 6a along the planes of surface plasmons quality, as the operational wavelength is being swept across the entire visible spectrum 400 nm $< \lambda < 700$ nm. Bilayers from Table 1 on maps with vertical axes representing the enhancement metric Q and horizontal axis measuring: (**a**) the plasmon wavenumber $\mathrm{Re}[\beta/k_0]$ and (**b**) the loss tangent $\tan \delta$. The optimal operational points are denoted by circular markers.

Figure 8. Trajectories of optimal designs from Fig. 6b along the planes of surface plasmons quality, as the operational wavelength is being swept across entire the visible spectrum 400 nm $< \lambda < 700$ nm. Bilayers from Table 2 on maps with vertical axes representing the enhancement metric Q and horizontal axis measuring: (**a**) the plasmon wavenumber $\mathrm{Re}[\beta/k_0]$ and (**b**) the loss tangent $\tan \delta$. The optimal operational points are denoted by circular markers.

Conclusion and discussion

Various metal/dielectric bilayers are located into a dense dielectric bath and get obliquely illuminated; in such a scenario, the magnetic field becomes maximized at the interface, leading to the development of surface plasmons. Therefore, one can identify which combinations of thicknesses and wavelengths provide strong local field enhancement and, accordingly, guidance of powerful surface waves. The followed process guarantees additionally minimum speed for the emerged surface plasmons or minimum attenuation as they propagate. Therefore, numerous optimal designs with several beneficial features (strong intensity, lossless, slow light) are obtained and can give extra degrees of freedom in the process of fabricating the respective setups.

An interesting expansion of the present work would be to consider metal/dielectric interfaces of finite extent able to host surface waves, incorporating cylindrical volumes[59,60]. In this way, the aim of inverse design for photonic metamaterials[61] will be well-served since the constituent bilayer meta-atom of the respective efficient structure would have been thoroughly optimized. Importantly, one can study additional components in the near field of the optimal bilayers[62,63], able to create the essential evanescent waves that excite the surface plasmons and demonstrate the performance superiority of the corresponding designs. Integral equations provide a versatile and powerful formulation tool that can encompass all the previous scenarios and can be treated with a variety of method: from semi-analytical expansions of scattering integral[64] and entire-domain basis functions[65] to surface current approximations[66]. Such extra steps will admit the analyzed structures to be tested as parts of more complex systems, where the increased field localization, the sharp spatial variation and the propagating qualities of surface plasmons, are vital.

Data availability

The datasets used and/or analysed during the current study available from the corresponding author on reasonable request.

References

1. Ritchie, R. H. Plasma losses by fast electrons in thin films. *Phys. Rev.* **106**, 874 (1957).
2. Turbadar, T. Complete absorption of light by thin metal films. *Proc. Phys. Soc.* **73**, 40 (1959).
3. Economou, E. N. Surface plasmons in thin films. *Phys. Rev.* **182**, 539 (1969).
4. Barchiesi, D., Otto, A. Excitations of Surface Plasmon Polaritons by Attenuated Total Reflection, revisited Riv. del Nuovo Cim. **36**, 173 (2013).
5. Kretschmann, E., & Raether, H. Radiative decay of non radiative surface plasmons excited by light. *Z. Naturforsch.* **23 a**, 2135 (1968).
6. Kretschmann, E. The determination of the optical constants of metals by excitation of surface plasmons. *Z. Phys.* **241**, 313 (1971).
7. Arakawa, E. T., Williams, M. W., Hamm, R. N. & Ritchie, R. H. Effect of damping on surface plasmon dispersion. *Phys. Rev. Lett.* **31**, 1127 (1973).
8. Ozbay, E. Plasmonics: Merging photonics and electronics at nanoscale dimensions. *Science* **311**, 189 (2006).
9. Homola, J., Yee, S. S. & Gauglitz, G. Surface plasmon resonance sensors: Review. *Sens. Actuators B* **54**, 3 (1999).
10. Redjem, W. et al. All-silicon quantum light source by embedding an atomic emissive center in a nanophotonic cavity. *Nat. Commun.* **14**, 3321 (2023).
11. Hutter, E. & Fendler, J. H. Exploitation of localized surface plasmon resonance. *Adv. Mater.* **16**, 1685 (2004).
12. Barnes, W. L., Dereux, A. & Ebbesen, T. W. Surface plasmon subwavelength optics. *Nature* **424**, 824 (2003).
13. Fang, N., Lee, H., Sun, C. & Zhang, X. Sub-diffraction-limited optical imaging with a silver superlens. *Science* **308**, 534 (2005).
14. Anker, J. N. et al. Biosensing with plasmonic nanosensors. *Nat. Mater.* **7**, 442 (2008).
15. Homola, J. Surface plasmon resonance sensors for detection of chemical and biological species. *Chem. Rev.* **108**, 462 (2008).
16. Jain, P. K., Huang, X., El-Sayed, I. H. & El-Sayed, M. A. Noble metals on the nanoscale: Optical and photothermal properties and some applications in imaging, sensing, biology, and medicine. *Acc. Chem. Res.* **41**, 1578 (2008).
17. Noguez, C. Surface plasmons on metal nanoparticles: The influence of shape and physical environment. *J. Phys. Chem. C* **111**, 3806 (2007).
18. Willets, K. A. & Van Duyne, R. P. Localized surface plasmon resonance spectroscopy and sensing. *Annu. Rev. Phys. Chem.* **58**, 267 (2007).
19. Moskovits, M. Surface-enhanced spectroscopy. *Rev. Mod. Phys.* **57**, 783 (1985).
20. Pendry, J. B., Martin-Moreno, L. & Garcia-Vidal, F. J. Mimicking surface plasmons with structured surfaces. *Science* **305**, 847 (2004).
21. Jablan, M., Buljan, H. & Soljačić, M. Plasmonics in graphene at infrared frequencies. *Phys. Rev. B* **80**, 245435 (2009).
22. Brongersma, M., Halas, N. & Nordlander, P. Plasmon-induced hot carrier science and technology. *Nat. Nanotechnol.* **10**, 25 (2015).
23. Zeng, S. et al. Graphene-MoS_2 hybrid nanostructures enhanced surface plasmon resonance biosensors. *Sens. Actuators B-Chem.* **207**, 801 (2015).
24. Rodrigo, D. et al. Mid-infrared plasmonic biosensing with graphene. *Science* **349**, 165 (2015).
25. Miao, J. et al. Surface plasmon-enhanced photodetection in few layer MoS_2 phototransistors with Au nanostructure arrays. *Small* **11**, 2392 (2015).
26. Xue, T. et al. Ultrasensitive detection of miRNA with an antimonene-based surface plasmon resonance sensor. *Nat. Commun.* **10**, 28 (2019).
27. Ding, X. G. et al. Surface plasmon resonance enhanced light absorption and photothermal therapy in the second near-infrared window. *J. Am. Chem. Soc.* **136**, 15684 (2014).
28. Huang, Y.-F. et al. Activation of oxygen on gold and silver nanoparticles assisted by surface plasmon resonances. *Angew. Chem. Int. Ed.* **53**, 2353 (2014).
29. Tang, W. et al. Broadband and high-efficiency excitation of spoof surface plasmon polaritons through rectangular waveguide. *Front. Phys.* **8**, 582692 (2020).
30. Chen, P. Y., Argyropoulos, C. & Alù, A. Enhanced nonlinearities using plasmonic nanoantennas. *Nanophotonics* **89**, 221 (2012).
31. Liu, W., Niu, Y., Luo, Z., & Li, M. Ultra electron density sensitivity for surface plasmons. arXiv:2307.04982 [physics.optics] (2023).
32. Garcia-Vidal, F. J. et al. Spoof surface plasmon photonics. *Rev. Mod. Phys.* **94**, 025004 (2022).
33. Achouri, K. & Caloz, C. Space-wave routing via surface waves using a metasurface system. *Sci. Rep.* **8**, 7549 (2018).
34. Martini, E., Mencagli, M. & Maci, S. Metasurface transformation for surface wave control. *Philos. Trans. R. Soc.* **373**, 20140355 (2015).
35. Huang, H. et al. Leaky-wave metasurfaces for integrated photonics. *Nat. Nanotechnol.* **18**, 580 (2023).
36. De Pineda, J. D., Ward, G. P., Hibbins, A. P. & Sambles, J. R. Metasurface bilayer for slow microwave surface waves. *Phys. Rev. B* **100**, 081409 (2019).
37. Baba, T. Slow light in photonic crystals. *Nat. Photon.* **2**, 465 (2008).
38. Krauss, T. F. Why do we need slow light?. *Nat. Photon.* **2**, 448 (2008).
39. Soljačić, M. et al. Photonic-crystal slow-light enhancement of nonlinear phase sensitivity. *J. Opt. Soc. Am. B* **19**, 2052 (2002).
40. Vlasov, Y. A., O'Boyle, M., Hamann, H. F. & McNab, S. J. Active control of slow light on a chip with photonic crystal waveguides. *Nature* **438**, 65 (2005).
41. Velten, A. et al. Recovering three-dimensional shape around a corner using ultrafast time-of-flight imaging. *Nat. Commun.* **3**, 745 (2012).
42. Papadimopoulos, A. N., Kantartzis, N. V., Tsitsas, N. L. & Valagiannopoulos, C. A. Wide-angle absorption of visible light from simple bilayers. *Appl. Opt.* **56**, 9779 (2017).
43. Valagiannopoulos, C. A. Arbitrary currents on circular cylinder with inhomogeneous cladding and RCS optimization. *J. Electromagn. Waves Appl.* **21**, 665 (2007).
44. Valagiannopoulos, C. A. Study of an electrically anisotropic cylinder excited magnetically by a straight strip line. *Prog. Electromagn. Res.* **73**, 297 (2007).
45. Kurman, Y. et al. Control of semiconductor emitter frequency by increasing polariton momenta. *Nat. Photon.* **12**, 423 (2018).
46. Iqbal, T. Propagation length of surface plasmon polaritons excited by a 1D plasmonic grating. *Curr. Appl. Phys.* **15**, 1445 (2015).
47. Naik, G. V., Shalaev, V. M. & Boltasseva, A. Alternative plasmonic materials: Beyond gold and silver. *Adv. Mater.* **25**, 3264 (2013).
48. Safavi-Naeini, A. H., Mayer Alegre, T.P., Chan, J., Eichenfield, M., Winger, M., Lin, Q., Hill, J.T., Chang, D. E., & Painter, O. Electromagnetically induced transparency and slow light with optomechanics. *Nature* **472**, 69 (2011).
49. Okawachi, Y. et al. Tunable all-optical delays via brillouin slow light in an optical fiber. *Phys. Rev. Lett.* **94**, 153902 (2005).

50. Lu, X., McClung, A. & Srinivasan, K. High-Q slow light and its localization in a photonic crystal microring. *Nat. Photon.* **16**, 66 (2022).
51. Kumar, A. et al. Slow light topological photonics with counter-propagating waves and its active control on a chip. *Nat. Commun.* **5**, 926 (2024).
52. Fang, Y. & Sun, M. Nanoplasmonic waveguides: Towards applications in integrated nanophotonic circuits. *Light Sci. Appl.* **4**, e294 (2015).
53. Zia, R., Schuller, J. A., Chandran, A. & Brongersma, M. L. Plasmonics: The next chip-scale technology. *Mater. Today* **9**, 21 (2006).
54. Cao, E., Lin, W., Sun, M., Liang, W. & Song, Y. Exciton-plasmon coupling interactions: From principle to applications. *Nanophotonics* **7**, 145 (2018).
55. Oulton, R. F., Sorger, V. J., Genov, D. A., Pile, D. F. P. & Zhang, X. Hybrid plasmonic waveguide for subwavelength confinement and long-range propagation. *Nat. Photon.* **2**, 496 (2008).
56. Maier, S. A. et al. Local detection of electromagnetic energy transport below the diffraction limit in metal nanoparticle plasmon waveguides Nat. *Mater.* **2**, 229 (2003).
57. Oulton, R. F. et al. Plasmon lasers at deep subwavelength scale. *Nature* **461**, 629 (2009).
58. Katsantonis, I. et al. Giant enhancement of nonreciprocity in gyrotropic heterostructures. *Sci. Rep.* **13**, 21986 (2023).
59. Valagiannopoulos, C. A. On measuring the permittivity tensor of an anisotropic material from the transmission coefficients. *Prog. Electromagn. Res. B* **9**, 105 (2008).
60. Valagiannopoulos, C. A. On smoothening the singular field developed in the vicinity of metallic edges. *Int. J. Appl. Electromagn. Mech.* **31**, 67 (2009).
61. Katsantonis, I., Droulias, S., Soukoulis, C.M., & Economou, E.N. Maria Kafesaki, PT-symmetric chiral metamaterials: Asymmetric effects and PT-phase control. *Phys. Rev. B* **101**, 214109 (2020).
62. Valagiannopoulos, C. A. On examining the influence of a thin dielectric strip posed across the diameter of a penetrable radiating cylinder. *Prog. Electromagn. Res. C* **3**, 203 (2008).
63. Alitalo, P., Valagiannopoulos, C. A. & Tretyakov, S. A. *Simple cloak for antenna blockage reduction* (IEEE International Symposium on Antennas and Propagation, 2011).
64. Valagiannopoulos, C. A. Closed-form solution to the scattering of a skew strip field by metallic pin in a slab. *Prog. Electromagn. Res.* **79**, 1 (2008).
65. Valagiannopoulos, C. A. & Tsitsas, N. L. Integral equation analysis of a low-profile receiving planar microstrip antenna with a cloaking superstrate. *Radio Sci.* **47**, 1 (2012).
66. Valagiannopoulos, C. A. Electromagnetic propagation into parallel-plate waveguide in the presence of a skew metallic surface. *Electromagnetics* **31**, 593 (2011).

Acknowledgements

Author contributions

K. Z. pursued her diploma thesis in the topic of the paper; she implemented the analytical method, produced the numerical results and drafted the manuscript. B. O. co-supervised the last phase of the project. C. V. performed the conceptualization, formal analysis and physical interpretation; he coordinated the execution of the project as well.

Declarations

Competing interests

The authors declare no competing interests.

Additional information

Correspondence and requests for materials should be addressed to B.O. or C.V.

Reprints and permissions information is available at www.nature.com/reprints.

Publisher's note Springer Nature remains neutral with regard to jurisdictional claims in published maps and institutional affiliations.